Numerical Study of the Optical Response of ITO-In_2O_3 Core-Shell Nanocrystals for Multispectral Electromagnetic Shielding

Nicola Curreli, *Member, IEEE*, Matteo Bruno Lodi, *Member, IEEE*, Michele Ghini, Nicolò Petrini, Andrea Buono, *Senior Member, IEEE*, Maurizio Migliaccio, *Fellow, IEEE*, Alessandro Fanti, *Senior Member, IEEE*, Ilka Kriegel, and Giuseppe Mazzarella, *Senior Member, IEEE*

***Abstract*—Nowadays, materials to protect equipment from unwanted multispectral electromagnetic waves are needed in a broad range of applications including electronics, medical, military and aerospace. However, the shielding materials currently in use are bulky and work effectively only in a limited frequency range. Therefore, nanostructured materials are under investigation by the relevant scientific community. In this framework, the design of multispectral shielding nanomaterials must be supplemented with proper numerical models that allow dealing with non-linearities and being effective in predicting their absorption spectra. In this study, the electromagnetic response of metal-oxide nanocrystals with multispectral electromagnetic shielding capability has been investigated. A numerical framework was developed to predict energy bands and electron density profiles of a core-shell nanocrystal and to evaluate its optical response at different wavelengths. To this aim, a finite element method software is used to solve a non-linear Poisson's equation. The numerical simulations allowed to model the optical response of ITO-In_2O_3 core-shell nanocrystals and can be effectively applied to different nanotopologies to support an enhanced design of nanomaterials with multispectral shielding capabilities.**

***Index Terms*—Computational electromagnetics, core-shell nanoparticles, lorentz-mie theory, multispectral shielding, plasmonic resonance.**

I. Introduction

THE development of electronic devices operating on a wide range of frequency from one side opened a plethora of new applications while, on the other side, came along with a substantial and critical rise of electromagnetic interference, *i.e.*, a set of unwanted collateral effects as device malfunctions and human exposure to electromagnetic radiation [1], [2]. To limit the impact of such unwanted effects, the interest and the demand for multispectral shielding materials grew exponentially in the last few years. Shielding materials that can successfully reduce the susceptibility to external radiation are needed in a broad set of applications as electronics medical, military and aerospace [3], [4], [5], [6], [7], [8]. For instance, smart electronics and telecommunication satellites operate in the dual-band spectrum of microwaves and infrared radiations [9], while medical equipment mostly work using microwaves and X-rays [10]. Additionally, the electromagnetic radiation emitted by the Sun covers a wide spectrum including microwave, infrared and ultraviolet wavelengths, which aerospace aircraft must cope with and endure [10]. Unfortunately, multispectral shielding requirements are not met by the shielding materials that are currently on the market, which are primarily synthesized for single-band electromagnetic waves. In fact, each band of the electromagnetic spectrum calls for unique attenuation mechanism [5], [11], [12], [13], [14]. Ultraviolet photons, for example, have enough energy to induce electron transitions between different energy levels (see Fig. 1). The wavelength of absorbed light has the energy required to promote an electron from a lower to a higher energy level resulting in the absorption of the ultraviolet photon. In this context, UV shielding materials are typically used in sunscreen applications since ultraviolet overexposure can harm living human cells [15], [16]. Considering military and security applications, infrared shielding or camouflage need for materials with

Manuscript received 15 October 2022; revised 12 December 2022; accepted 5 January 2023. Date of publication 10 January 2023; date of current version 2 February 2023. The work of Nicola Curreli, Michele Ghini, Nicolo Petrini, and Ilka Kriegel was supported in part by European Union's Horizon 2020 European Research Council, under Grant 850875 (Ilka Kriegel) (Light-DYNAMO), and in part by European Union's Horizon 2020 Research and Innovation Program under Grant 101017821 (Ilka Kriegel) (LIGHT-CAP). The work of Matteo Bruno Lodi, Giuseppe Mazzarella, and Alessandro Fanti was supported by the Ministero dello Sviluppo Economico, in AGRIFOOD Programma Operativo Nazionale (PON) Imprese e Competitività (I&C) 2014–2020, through Project "Ingegnerizzazione e Automazione del Processo di Produzione Tradizionale del Pane Carasau mediante l'utilizzo di tecnologie IoT (IAPC)," under Grants CUP: B21B19000640008 and COR: 1406652. *(Nicola Curreli and Matteo Bruno Lodi contributed equally to this work.) (Corresponding authors: Nicola Curreli; Alessandro Fanti.)*

Nicola Curreli and Nicolò Petrini are with Functional Nanosystems, Italian Institute of Technology, 16163 Genova, Italy, and also with Molecular Foundry, Lawrence Berkeley National Laboratory, Berkeley, CA 94720 USA (e-mail: nicola.curreli@iit.it; nicolo.petrini@iit.it).

Matteo Bruno Lodi, Alessandro Fanti, and Giuseppe Mazzarella are with the Department of Electrical and Electronic Engineering, University of Cagliari, 09123 Cagliari, Italy, and also with the National Inter-University Consortium for Telecommunications (CNIT), University of Cagliari Research Unit, 09123 Cagliari, Italy (e-mail: matteobrunolodi@ieee.org; alessandro.fanti@diee.unica.it; mazzarella@unica.it).

Michele Ghini is with Functional Nanosystems, Italian Institute of Technology, 16163 Genova, Italy, and also with Nanoelectronic Devices Laboratory, Ecole Polytechnique Fédérale de Lausanne, 1015 Lausanne, Switzerland (e-mail: michele.ghini@epfl.ch).

Andrea Buono and Maurizio Migliaccio are with Dipartimento di Ingegneria, Università degli Studi di Napoli "Parthenope," 80133 Napoli, Italy (e-mail: andrea.buono@uniparthenope.it; maurizio.migliaccio@uniparthenope.it).

Ilka Kriegel is with Functional Nanosystems, Italian Institute of Technology, 16163 Genova, Italy (e-mail: ilka.kriegel@iit.it).

This article has supplementary downloadable material available at https://doi.org/10.1109/JMMCT.2023.3235750, provided by the authors.

Digital Object Identifier 10.1109/JMMCT.2023.3235750

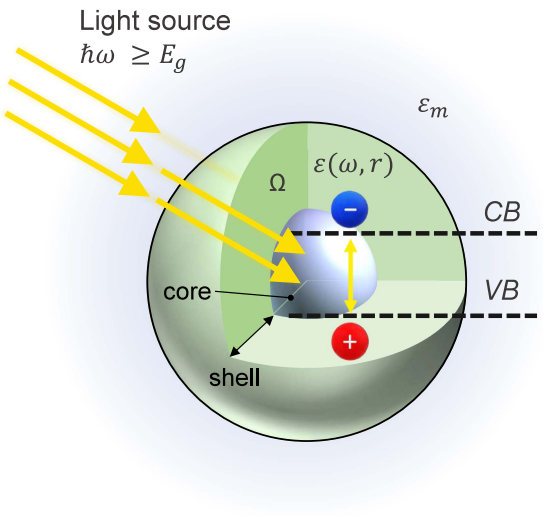

Fig. 1. Schematics of a metal-oxide nanocrystal (NC), in which it is evidenced the core-shell structure and the effect of photodoping with a sufficent energetic photon able to induce photogeneration of carriers.

low infrared emissivity and low thermal conductivity [17]. The former, according to Kirchhoff's equation of thermal radiation for opaque materials, can be attained by high reflectivity, which in turn depends on electrical conductivity [18].

In this framework, the study of nanoscale radiators, scatterers and absorbers is a fundamental challenge to enable industrial and biomedical plasmonic applications [19]. Nonetheless, the design of nanomaterials with suitable properties must be supported with proper theoretical and numerical tools. To date, the literature focused on the analytical analysis of metallic, spherical nanoparticles under resonance conditions [20], especially considering scattering [21], [22], [23]. By solving the full dipole equation for the dominant mode radiation damping of the oscillating nanocrystal (NC), closed-form equations to study the near- or far-field characteristics can be derived. Several models have been developed to quantitatively describe the resonant behavior of NC (radii from 5 nm to 50 nm), through lumped-impedance representation based on the quasi-static approximation [24], [25]. The latter holds, depending on the scatterer size, the radiation wavelength and the field homogeneity in the nanoparticle [26]. The classic circuit concept, which is limited to the fundamental dipole mode, could be extended to predict the optical spectrum of nanoparticles independently on wavelength, size and material properties constraints [27]. Further efforts, such as the closed-form solution from [28], were spent in accounting for third order non-linear susceptibility in metallic nanostructures. However, when quasi-static approximation and circuital models do not apply, *i.e.*, when high non-linearities are in place, numerical methods to investigate the interaction between the electromagnetic radiation and the NC are adopted [29]. For instance, recently, in [30], the surface enhanced Raman scattering of multiple nanostructures was studied by developing a wide-band nested equivalent source approximation accelerated method of moments. Finite element method (FEM) solvers, in particular, have been assessed to be effective numerical tools to investigate the performance of absorbing nanostructures [29], [31], [32]. So far, the studies about the numerical analysis of innovative nanomaterials mostly dealt with scattering, focusing with noble metals (*e.g.*, gold nanosphere) [29] or dielectric nanoparticles [23], and core-shell systems have been understudied [22]. There is lack of numerical framework capable of handling extinction and scattering mechanisms of nanomaterials. Furthermore, any of the aforementioned models can predict the multispectral optical response of nanomaterials starting from their electronic properties.

In this study, we adopted numerical tools to simulate the electromagnetic response of metal oxide nanocrystals (MO-NCs) with multispectral shielding capabilities. Based on different principles, effective shielding can be achieved by core-shell MO-NCs in a wide range of frequencies, from infrared to ultraviolet. Despite several plasmonic semiconductors can be used for shielding applications (Fig. S1, Supplementary Material) [33], [34], [35], $Sn : In_2O_3$-In_2O_3 (ITO-In_2O_3) NCs were considered as a case study due to their relative ease in the synthesis of core-shell structures. We first modeled an isolated core-shell NCs, pre- and post-photodoping, to account for their optical response by performing full-field optical simulations using steady state carrier concentration profiles. The latter are obtained by solving Poisson's equation over a spherical NC. Then, we predicted their far-field optical response and analyzed the near-field characteristics around the NCs.

II. Electrostatic Simulations

In this section, a three-dimensional model of a single NC is presented assuming an uniform dopant concentration from the center up to the interface between the core and shell regions. Charges in surface states are considered to be located outside the NC. To obtain the electric field at the surface, the Poisson's equation must be integrated from the center to the surface of the NC.

A. General Model

The Poisson's equation is defined as [36]:

$$\nabla^2 u = -\frac{e^2}{\varepsilon_\infty(r)\varepsilon_0 k_B T}\,\rho(r) \tag{1}$$

where $\varepsilon_\infty(r)$ and ε_0 are the high-frequency dielectric permittivity of the NC and the permittivity of free space, respectively. To integrate Poisson's equation, an explicit expression for the charge density at any point, $\rho(r)$, is needed, which is given by [36], [37]:

$$\rho(r) = p_h - n_e + \rho_D(r) + \rho_A(r) \tag{2}$$

where p_h and n_e are the carrier density contribution of mobile electrons and holes, respectively, $\rho_D(r)$ and $\rho_A(r)$ are the radially changing donor and acceptor dopant density, respectively, while e is the unit electron charge. In the following, energy and potential terms are indicated as follows: E_F is the Fermi energy while E_C and E_V are the energies at the bottom of the conduction band (CB) and the top of the valence band (VB), respectively. For the sake of convenience, it has been defined an

intrinsic energy E_I, which is defined as $\frac{E_C+E_V}{2}$. At any point r in the NC, it is possible to define a generic potential [38]:

$$w_{P,Q} = \frac{E_P - E_Q}{k_B T} \tag{3}$$

where E_P and E_Q are two generic energy levels. In particular, the dimensionless potential u between E_F and E_I is defined as:

$$u = \frac{e\varphi}{k_B T} \tag{4}$$

where k_B is the Boltzmann constant, T is the temperature and φ is the potential difference:

$$\varphi = \frac{E_F - E_I}{e} \tag{5}$$

At any point inside the NC, the electron volume density, n_e is given by [38]:

$$n_e = 2\int_{E_C}^{E_{CU}} D_C(E)\cdot f(E)dE \tag{6}$$

where E_{CU} is the upper edge of the CB, $D_C(E)$ is the density of states, which is the number of states per unit energy per unit volume [38]:

$$D_C(E) = 4\pi\left(\frac{2m_e^*}{h^2}\right)^{\frac{3}{2}}(E-E_C)^{\frac{1}{2}} \tag{7}$$

where h is the Planck's constant, m_e^* is the effective electron mass in the CB which is equal to 0.4 times the electron mass in the case of ITO and In_2O_3 [36], while $f(E)$ is the Fermi-Dirac distribution function given by [38]:

$$f(E) = \left(1+\exp\left(\frac{E-E_F}{k_B T}\right)\right)^{-1} \tag{8}$$

The use of the density of states expression for bulk structures is justified by the absence of quantum confinement effects (discussion in Supplementary Material). In (6), the factor two in front of the integral is due to the fact that each state in the CB can host two electrons of opposite spin. It must be highlighted that, usually, the integration limit E_{CU} is replaced with $+\infty$ to account for the fact that the integrating function vanishes exponentially at high energies. To compute this term, approximated expressions are used [37]. However, in this case, we selected this value iteratively by looking for a value large enough to ensure the convergence to a solution and to achieve an accuracy no larger than 1%. By replacing (7) and (8) into (6), we get:

$$n_e = 4\pi\left(\frac{2m_e^*}{h^2}\right)^{\frac{3}{2}}\int_{E_C}^{E_{CU}}\frac{(E-E_C)^{\frac{1}{2}}}{1+\exp\left(\frac{E-E_F}{k_B T}\right)}dE \tag{9}$$

Rearranging (9), we obtain:

$$n_e = 4\pi\left(\frac{2m_e^* k_B T}{h^2}\right)^{\frac{3}{2}} F_{\frac{1}{2}}(u - w_{C,I}) \tag{10}$$

where $F_j(\eta)$ is the integral Fermi-Dirac function defined as [39]:

$$F_j(\eta) = \int_{E_Q}^{E_P}\frac{x^j}{1+\exp(x-\eta)}dx \tag{11}$$

being $j \in \mathbb{Z}^+$, η and x the variable and the dummy term, respectively.

Similarly, the hole volume density in the VB, p_h, is [38]:

$$p_h = 2\int_{-\infty}^{E_V} D_V(E)\left[1-f(E)\right]dE \tag{12}$$

where $D_V(E)$ is the number of quantum states in the VB per unit energy per unit volume, which is given by [38]:

$$D_V(E) = 4\pi\left(\frac{2m_h^*}{h^2}\right)^{\frac{3}{2}}(E_V - E)^{\frac{1}{2}} \tag{13}$$

where m_h^* is the hole's effective mass in the VB equal to 0.6 times the electron mass in the case of ITO and In_2O_3 [36]. In (12), the lower integration limit is taken to -∞ based on the assumption that E_F is several $k_B T$ above the bottom of the VB. Finally, by inserting (8) and (13) in (12), we obtain:

$$p_h = 4\pi\left(\frac{2m_h^* k_B T}{h^2}\right)^{\frac{3}{2}} F_{\frac{1}{2}}(w_{V,I} - u) \tag{14}$$

Once the electron and hole densities are obtained, to determine the charge density in any point (see (2)), information on the charge concentration due to ionized impurities is needed. We assumed that the impurity concentration is sufficiently low to consider the occupation of each site independently, *i.e.*, the states are non-interacting. Under this assumption, a simple model for donors and acceptors can be used. Donors are considered neutral impurity atoms, each of which can release an unpaired electron thus becoming positively charged; while acceptors are atoms of impurities that can gain an electron (which goes into a coupled state) thus becoming negatively charged. Given the energy level and the concentration of the donors, E_D and N_D, respectively, the concentration of electrons in donor sites can be found as [40]:

$$\rho_D = N_D\left(1+2\exp\left(\frac{E_F - E_D}{k_B T}\right)\right)^{-1} \tag{15}$$

where the coefficient 2 in (15) is the ground-state degeneracy of the donor impurity due to the possibility for the electron occupying a given donor site to be of either spin [37], [41], which can be rewritten in terms of potentials:

$$\rho_D = N_D\left(1+2\exp\left(u - w_{D,I}\right)\right)^{-1} \tag{16}$$

The expression for the occupation of the acceptor sites can be found similarly to (15), just considering that, in this case, the electron must be paired [37], [41]. The acceptor electron energy, E_A, and the concentration of acceptor sites, N_A, can be combined to obtain the concentration of electrons in acceptor sites, ρ_A:

$$\rho_A = N_A\left(1+2\exp\left(\frac{E_A - E_F}{k_B T}\right)\right)^{-1} \tag{17}$$

Again, in terms of potentials, we have:

$$\rho_A = N_A\left(1+2\exp\left(w_{A,I} - u\right)\right)^{-1} \tag{18}$$

TABLE I
PARAMETERS USED IN THE SIMULATIONS.

Parameter (unit)	Value
e (C)	$1.602 \cdot 10^{-19}$
ε_0 (Fm^{-1})	$8.854 \cdot 10^{-12}$
k_B (JK^{-1})	$1.381 \cdot 10^{-23}$
T (K)	293.15
m_h^* (kg)	$5.466 \cdot 10^{-31}$
m_e^* (kg)	$3.644 \cdot 10^{-31}$
h (Js)	$6.626 \cdot 10^{-34}$
$N_{\max}$	4000
σ_f	5.5

TABLE II
NON-EQUILIBRIUM CB AND VB LEVELS FOR ITO AND In_2O_3 [36].

Material	CB minimum (eV)	VB maximum (eV)	Intrinsic level (eV)
ITO	1.8758	-1.8758	0
In_2O_3	2.1768	-1.8238	0.1765

Finally, by inserting (2) in (1) and replacing (10), (14), (16), (18) in (2), then (1) reads as:

$$\nabla^2 u = -\frac{e^2}{\varepsilon_\infty(r)\varepsilon_0 k_B T}\left(\frac{N_D}{1+2\exp\left(u-w_{D,I}\right)}+\right.$$
$$-\frac{N_A}{1+2\exp\left(w_{A,I}-u\right)}$$
$$+4\pi\left(\frac{2m_h^* k_B T}{h^2}\right)^{\frac{3}{2}} F_{\frac{1}{2}}\left(w_{V,I}-u\right)+$$
$$\left.-4\pi\left(\frac{2m_e^* k_B T}{h^2}\right)^{\frac{3}{2}} F_{\frac{1}{2}}\left(u-w_{C,I}\right)\right). \quad (19)$$

B. Pre-Photodoped NCs

When dealing with spherical NCs, we solved numerically the Poisson's equation (19) using the built-in Mathematics module of the Comsol Multiphysics v5.6 (Comsol Inc., Burlinghton, MA, USA) FEM software. The variable is discretized by using quadratic Lagrange element and a free triangular mesh is used in the NC analysis domain. The built-in Multifrontal Massively Parallel sparse direct Solve tool, with a non-linear Newton solver is adopted, with pivoting, row pre-ordering, an initial damping factor $\tau_d = 10^{-4}$ and a maximum number of iterations $N_{\text{iter}} = 10^3$. Numerical simulations are run setting the parameters according to [42], see Table I.

The non-equilibrium CB minimum (E_C), VB maximum (E_V) and intrinsic band (E_I) levels for ITO and In_2O_3 used in the simulations are listed in Table II, where $E_I = 0$ eV is set for ITO as a reference.

In the case of NCs consisting of a single material only (ITO NCs), energy levels, number and concentration of donors, relative dielectric permittivity and high-frequency dielectric permittivity are spatially constant. For a combination of different materials (ITO-In_2O_3 core-shell NCs), we modeled the elemental composition of the materials by introducing a radial-dependent permittivity profile ($\varepsilon_\infty(r)$), non-equilibrium bandgap energy ($E_g = E_C - E_V$), and a radial-dependent donor distribution

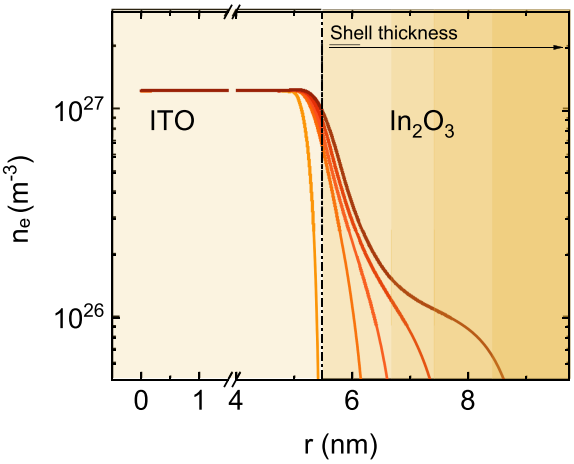

Fig. 2. Electron density profiles in a core-shell structure of ITO-In_2O_3 with $R_{core} = 5.5$ nm and different shell thickness ($t_s = 0$ nm, 1 nm, 2 nm, 3 nm and 4 nm). .

profile ($N_D = N_D(r)$) to take into account the material-dependence of the NCs. In our case, the diffusion effects on the ITO-In_2O_3 core-shell NCs are investigated by introducing two different donor concentration levels for ITO and In $_2$ O_3, $N_{D,\text{core}}$ and $N_{D,\text{shell}}$, respectively. Therefore, we considered the donor distribution profile as follows:

$$N_D(r) = N_{D,\text{shell}} + \frac{N_{D,\text{core}}}{1+\exp\left(k_{\text{sh}}(r-R_{\text{core}})\right)} \quad (20)$$

where $N_{D,\text{shell}} = 10^{21}$ m^{-3}, $N_{D,\text{core}} = 10^{26}$ m^{-3} are taken from experimental data in [36], and $R_{\text{core}} = 5.5$ nm is the radius of the core. Different shape factors, *i.e.*, $k_{\text{sh}} = 5, 25$ and 100, are considered in solving the Poisson's equation. This analysis pointed out that differences in the electron density profiles are negligible for different $k_{\text{sh}} > 1$ The spatially-dependent carrier density profile, *i.e.*, $n_e(r)$, inside a NC is first solved for different parameters, see Fig. 2. As previously reported in [36], the effect of the Fermi level pinning on the equilibrium conduction band profile is modelled by considering different fixed NC surface states (E_S) and introducing additional electronic interfaces (core-shell system).

We found that $n_e(r)$ is enough to completely suppress the metallic behavior of carriers close to the NC surface (Fig. 2). According to the surface level pinning E_S, the carrier density profile at the surface determines a region depleted of carriers, which effectively suppresses the metallic behaviour at the surface, thus confining the free electrons in an inner region. As a result, this depletion region effectively acts as a dielectric. When E_S increases from 0 eV to 2 eV, we observed an increase in the depletion layer width, which affects a larger fraction of the NC volume. The introduction of a shell layer with different thicknesses (t_s) which acts as an additional electronic interface beyond the surface of the nanoparticle, is another parameter that allows controlling the depletion layer and the carrier density profiles. Fig. 2 shows the tuning of the carrier density profile in the ITO-In_2O_3 core-shell NC system. Here, $E_S = 2$ eV is

set [36]. It is important to underline that, in the core-shell system under analysis, two electronic interfaces occur: ITO-In_2O_3 and In_2O_3- NC surface. While in uniform NCs, *i.e.*, $t_s = 0$ nm, the carrier density profile is determined by the radial depletion region near the NC surface, the addition of a shell layer with increasing thickness modifies the depletion layer resulting in a double-bent carrier density profile. With increasing t_s, a more pronounced bending of the carrier density distribution is observed, showing a non-trivial profile. The double bending can be explained by a redistribution of free carriers into the shell, while the donor sites $N_D(r)$ remain fixed. The carrier density in large regions of the undoped shell (In_2O_3) reaches values larger than 10^{26} m^{-3}. These effects can be further extended by introducing different materials or by combining several materials together in other core-shell NCs structures and/or multiple materials sequentially in core-multishell NC architectures [36].

C. Post-Photodoped NCs

In this subsection, the electronic structure of core-shell NCs is investigated out of the equilibrium conditions by introducing multiple free-charge carriers with photodoping [16], [43], [44], [45]. This analysis aims to determine the effect of photodoping on the carrier density distribution of the system. In this way, we go beyond the results shown in Fig. 2 while assessing the dynamic, post-synthetic variation of the carrier density profiles via light-induced charge injection (photodoping). Hence, taking into account the ITO-In_2O_3 system, we solved Poisson's equation with the numerical methods introduced before. The effect of the photodoping is intended to be an "on-off" effect that does not depend on the frequency of the impinging source. For this reason, we simply included additional generation ($G(r)$) and recombination ($R(r)$) wavelength-independent terms into the Poisson's equation [46]:

$$\nabla^2 u = -\frac{e}{\varepsilon_\infty(r)\varepsilon_0 k_B T}\rho(r) + G(r) - R(r) \tag{21}$$

Notably, the recombination effects are neglected, *i.e.*, $R(r) = 0$, since the media surrounding the NC acts as an hole scavenger suppressing carrier recombination [36]. On the other hand, the generation term $G(r) \neq 0$ extends the Poisson's equation representing the spatial distribution of the extra free carriers introduced into the system via photodoping. The generation term can be modelled by the following Gaussian distribution [46]:

$$G(r) = \frac{N_{\max}}{V} \cdot \frac{1}{\sigma_f\sqrt{2\pi}} \exp\left(\frac{r - R_{\mathrm{NC}}}{\sigma_f}\right) \tag{22}$$

where $N_{\max}$ is the peak number of photoelectrons introduced, V is the volume of the NC, σ_f is the shape factor that rules the spatial distribution of the photoelectrons into the NC, whose radius is R_{NC}. Here, the terms $N_{\max}$ and σ_f have been derived from experimental results in [36], [42]. In particular, the σ_f term is numerically tuned to reduce the discrepancy with the experimental findings reported in [36].

The comparison of the carrier density profiles both pre- and post-photodoping is shown in Fig. 3. Similarly to the non-photodoped case discussed in section II-B, when increasing t_s a bending of the carrier density distribution occurs and

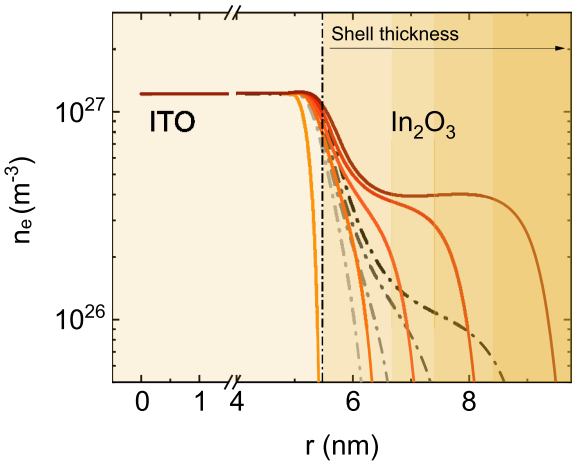

Fig. 3. Electron density profiles simulated for a ITO-In_2O_3 NC with R_{core} = 5.5 nm and different shell thickness (t_s = 0 nm, 1 nm, 2 nm, 3 nm and 4 nm) pre- (dotted lines) and post- (solid lines) photodoping. The largest variations in n_e post-photodoping occur towards the edge region of the NC with a significant rise of carrier density in the shell region.

the observed double bending becomes more pronounced upon photodoping in all samples, thus affecting the carrier density distribution. Indeed, post-photodoping, for samples calling for $t_s > 2.7$ nm, the carrier density profile approaches a step function with two distinct density levels in a two-step profile. The maximum n_e achieved in the NC shell differs from the one in the core, reaching values of around $4 \cdot 10^{26}$ m^{-3}, while the carrier density in the core remains almost constant.

III. Optical Simulation

We assume a time-harmonic plane wave excitation, linearly polarized along the x-direction while propagating along the z-axis, with intensity of 1 Vm^{-1}, that impinges a penetrable object placed in a bounded 3D domain Ω. In the latter, both outside and inside regions Maxwell's equations are satisfied (Fig. 1). The dielectric properties, *i.e.*, the space-dependent complex permittivity of the space, are defined as:

$$\begin{aligned} \varepsilon(r) &= \varepsilon_m\varepsilon_0 \text{ outside } \Omega \\ \varepsilon(r) &= \varepsilon_r(r)\varepsilon_0 \text{ in } \Omega \end{aligned} \tag{23}$$

where $\varepsilon_m = 2.27$ is the relative permittivity of the surrounding medium (toluene) [42] and $\varepsilon_r(r)$ is the space-dependent complex permittivity:

$$\varepsilon_r(r) = \varepsilon_r'(r) - i\varepsilon_r''(r) \tag{24}$$

where $\varepsilon_r'(r) = \Re\{\varepsilon_r(r)\}$ and $\varepsilon_r''(r) = \Im\{-\varepsilon_r(r)\}$ are the real and the imaginary part of the complex permittivity, respectively. By considering the analytical solution of Maxwell's equations in the case of an electromagnetic field interacting with a spherical particle, it is possible to derive a set of field expressions expanded in the spherical coordinate system [23]. From the Lorenz-Mie wavelength-dependent complex scattering electric (a_q) and magnetic (b_q) coefficients, it is possible to rigorously quantify the NC electric properties and size contributions to

the overall scattering behavior. The determination of a_q and b_q coefficients requires the solution of the boundary value problem, *i.e.*, the continuity of all the components of the tangential field at the interface, assuming that the solutions consists of functions that vanish at infinity. The a_q and b_q coefficients are described by a set of functions that consists of a combination of spherical Riccati–Bessel ($\psi_q = xj_q(x)$) and Riccati–Hankel ($\xi_q = xh_q^{(1)}(x)$) functions of the first kind:

$$a_q = \frac{m\psi_q(mkr)\psi_q'(kr) - \psi_q(kr)\psi_q'(mkr)}{m\psi_q(mkr)\xi_q'(kr) - \xi_q(kr)\psi_q'(mkr)}$$
$$b_q = \frac{\psi_q(mkr)\psi_q'(kr) - m\psi_q(kr)\psi_q'(mkr)}{\psi_q(mkr)\xi_q'(kr) - m\xi_q(x)\psi_q'(mkr)} \quad (25)$$

where the superscript $'$ means derivative with respect to the dummy variable x, q is the order of the Bessel function, k is the wavenumber of the impinging light and m is the relative complex refractive index, defined as:

$$m^2 = (\nu - i\kappa)^2 = \frac{\varepsilon_r}{\varepsilon_m} \quad (26)$$

where ν is the refractive index and κ is the extinction coefficient. To describe the energy balance between the scattering and extinction mechanisms within Ω, the far-field scattering and extinction cross-section efficiencies are typically considered. The extinction (Q_{ext}), scattering (Q_{sca}) and absorption (Q_{abs}) cross-sections can be expressed as a combination of the Lorenz-Mie coefficients as follows:

$$Q_{\text{ext}} = \frac{2\pi}{k^2}\sum_{q=1}^{+\infty}(2q+1)\,\Re\{a_q + b_q\}$$
$$Q_{\text{sca}} = \frac{2\pi}{k^2}\sum_{q=1}^{+\infty}(2q+1)\left(|a_q|^2 + |b_q|^2\right)$$
$$Q_{\text{abs}} = Q_{\text{ext}} - Q_{\text{sca}} \quad (27)$$

First, we evaluated the ratio between the absorption and scattering coefficients ($Q_{\text{abs}}/Q_{\text{sca}}$) for uniform ITO NCs with $n_e = 10^{27}$ m^{-3} having a radius varying from 1 nm to 20 nm and considering a wavelength dependent response between 290 nm and 2000 nm. For every point of the NC, the resonant condition for the plasmonic peak can be obtained from the complex-valued dielectric function of the NC, which is given by a Drude model:

$$\varepsilon(\omega, r) = \varepsilon_\infty(r) - \frac{\omega_p^2(r)}{\omega^2 + i\omega\gamma(r)} \quad (28)$$

where $\omega_p = \sqrt{\frac{n_e(r)e^2}{\varepsilon_0 m_e^*}}$ is the bulk plasma frequency and $\gamma(r)$ is a damping term that provides the free-electron description inside the NC. The frequency-radial distribution of the complex electric permittivity simulated for the considered NCs is shown in Fig. S2 (Supplementary Material), where panels a, b, e and f (c, d, g and h) refer to pre-photodoped and post-photodoped NCs, respectively. In the range of values spanning between -135 $< \varepsilon_r' <$ 5 and -370 $< \varepsilon_r'' <$ 0 we found that by setting $q = 10$ in (27), $Q_{\text{sca}} << Q_{\text{abs}}$ applies within our range of interest. This means that the scattering contribution to the optical response can be neglected (*i.e.*, extinction and absorption components

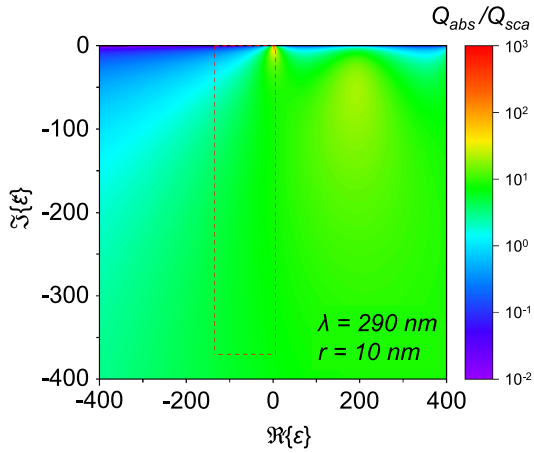

Fig. 4. Ratio between the absorption and scattering coefficients by varying real and imaginary parts of the complex permittivity of a single nanocrystal when the wavelenght of the incident light is 290 nm and the radius of the NC is $r = 10$ nm. The red dashed box highlight range of the values considered in this study.

are equivalent). In addition, for the range of r and k values considered in this work, *i.e.*, $r \cdot k \leq 1$, the extinction and scattering cross-sections reduces to the first term of the series (27). The latter is a sufficient condition to describe the dissipation of light by absorption and scattering, which in the case of linear regime of $r \cdot k$ limits to the well-known relationship for Rayleigh scattering [47]. Hence, it can be stated that scattering is negligible and the extinction can be approximated with the absorption. Moreover, it is possible to highlight that, although in the range of ε_r values obtained for the NCs under investigation (see the area bounded by the red dashed box in Fig. 4) the absorption process dominates over the scattering one. Prospectively, it would be interesting to study materials calling for $\varepsilon_r' > 0$ as they present resonances where absorption is even more efficient. For this reason, it has been evaluated $Q_{\text{abs}}/Q_{\text{sca}}$ by varying real and imaginary parts of the complex electric permittivity in the range [-400, 400] while setting the NC radius and the wavelength of the incident light $r = 10$ nm and $\lambda = 290$ nm ($\lambda = \frac{1}{k}$), see Fig. 4. From the latter analysis, it is straightforward to observe that by varying ε_r, the absorption-to-scattering ratio is dominated by the absorption, even in the limit case for which $\frac{r}{\lambda} = 0.03$.

A. Power Balance Model

In this subsection, we evaluated the near- and far-field responses of the NCs under analysis with the purpose of correlating their carrier concentration profiles and their optical properties. Indeed, owing to the proportionality between ω_p and n_e, the plasmonic resonances represent a source of information for the doping processes occurring in NCs [48], [49], [50]. In fact, at the interface between the NCs and the medium, the real part of the dielectric function changes sign across the interface, thus showing coherent delocalized electron oscillations (*i.e.*, surface plasmons). In NCs of size comparable to or smaller than the wavelength of light used to excite the plasmon, a localized surface plasmon (LSP) occurs, as a result of the confinement of a surface plasmon. In resonance conditions, the coupling of the incident radiation with LSP leads to a loss of energy when

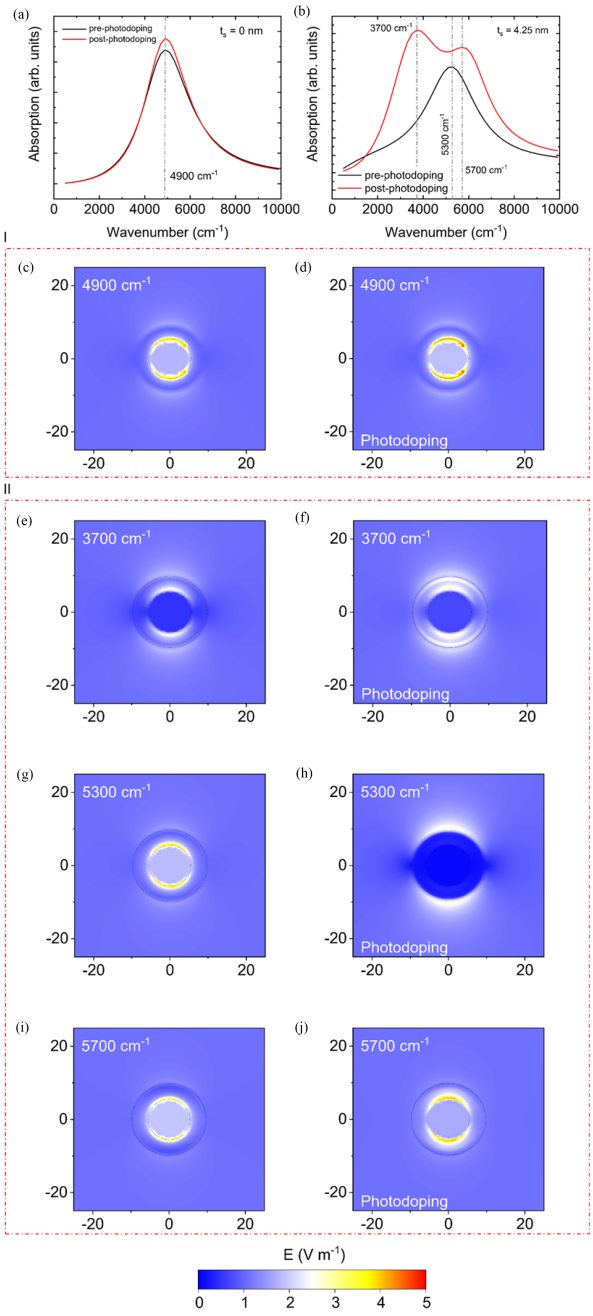

Fig. 5. Simulated absorption spectra (a and b) and electric field distribution (c-j) of the NC under analysis. Panels a and b refer to pre-photodoped (black line) and post-photodoped (red line) ITO NC consisting of the core only ($t_s = 0$ nm) and to pre-photodoped (black line) and post-photodoped (red line) ITO-In $_2$ O$_3$ core-shell NC with $t_s = 4.25$ nm. Panels from c and d refer to the electric field distribution (in Vm $^{-1}$) at 4900 cm^{-1} for the only core NC and the core-shell NC, respectively. Panels e, g and i refer to the electric field patterns of the ITO NC at $\omega = 3700$ cm^{-1}, 5300 cm^{-1} and 5700 cm^{-1}, respectively, while panels f, h and j refer to the electric field patterns of the ITO-In$_2$ O$_3$ ($t_s = 4.25$ nm) core-shell NC at $\omega = 3700$ cm^{-1}, 5300 cm^{-1} and 5700 cm^{-1}.

transmitted to the plasmons, resulting in a maximum absorption. Frequencies of light below the resonance are reflected by a material because the electrons in the material screen the electric field of the light. This principle can be used for shielding purposes. Hence, we coupled the radial carrier distribution already obtained by solving numerically the non-linear Poisson's equation with the high-frequency formulation of Maxwell's equation relating the carrier density of the NCs to the plasmonic resonance and simulating the absorption spectra. The frequency-domain equations are given by the lossy Helmholtz's wave equations:

$$\nabla^2\mathbf{E} + (\mu\varepsilon\omega^2 - i\mu\sigma\omega)\mathbf{E} = 0$$
$$\nabla^2\mathbf{H} + (\mu\varepsilon\omega^2 - i\mu\sigma\omega)\mathbf{H} = 0 \tag{29}$$

where σ is the electric conductivity and μ is the magnetic permeability. The power associated to the electromagnetic wave traveling into (or radiated from) the NC (inside the Ω domain) can be expressed as a flux integral of the inward-directed (or outward-directed) normal component of the Poynting vector over the surface $\partial\Omega$ [51], [52]. In addition, similar expressions can also be derived for scattered and extinguished power by integrating the associated components of the Poynting vector. First, the time average Poynting vector can be decomposed into its total time-harmonic field ($\mathbf{E}$, $\mathbf{H}$) components [51], [52]:

$$\mathbf{S}_{\text{tot}} = \frac{1}{2}\mathbf{E}_{\text{tot}} \times \mathbf{H}^*_{\text{tot}} = \mathbf{S}_{\text{tot}} = \mathbf{S}_{\text{inc}} + \mathbf{S}_{\text{sca}} + \mathbf{S}_{\text{ext}} \tag{30}$$

where $\mathbf{S}_{\text{inc}}$, $\mathbf{S}_{\text{sca}}$ and $\mathbf{S}_{\text{ext}}$ represent incident, scattered and extinguished components, respectively, where

$$\mathbf{S}_{\text{inc}} = \frac{1}{2}\mathbf{E}_{\text{inc}} \times \mathbf{H}^*_{\text{inc}} \tag{31}$$

$$\mathbf{S}_{\text{sca}} = \frac{1}{2}\mathbf{E}_{\text{sca}} \times \mathbf{H}^*_{\text{sca}} \tag{32}$$

$$\mathbf{S}_{\text{ext}} = \frac{1}{2}\left(\mathbf{E}_{\text{sca}} \times \mathbf{H}^*_{\text{inc}} + \mathbf{E}_{\text{inc}} \times \mathbf{H}^*_{\text{sca}}\right) \tag{33}$$

Please note that, here, the incident fields ($\mathbf{E}_{\text{inc}}$, $\mathbf{H}_{\text{inc}}$) are the fields generated by the sources in the absence of the scatterer. Then, it is possible to derive the relations needed to evaluate the absorbed, extinguished, scattered and radiated powers. The absorbed power is defined as the power traveling into the NC and is given by the integral of the inward-directed normal component of the Poynting vector. By applying Poynting's theorem and the divergence theorem, the absorbed power in terms of volumetric quantities is found as follows:

$$P_{\text{abs}} = -\oiint_{\partial\Omega} \mathbf{S}_{\text{tot}} \cdot \hat{\mathbf{n}} \tag{34}$$

where $\hat{\mathbf{n}}$ is the outward-directed surface normal. The power associated to the extinction process is the total power removed from the incident field (*i.e.*, the sum of the absorbed and the scattered powers) due to the presence of the NC. As for the extinction power, it can be obtained as:

$$P_{\text{ext}} = -\oiint_{\partial\Omega} \mathbf{S}_{\text{ext}} \cdot \hat{\mathbf{n}} \tag{35}$$

Finally, the power scattered from the NC is given by the integral of the outward-directed normal component of S_{sca} over $\partial\Omega$:

$$P_{\text{sca}} = -\oiint_{\partial\Omega} \mathbf{S}_{\text{sca}} \cdot \hat{\mathbf{n}} \tag{36}$$

Hence, according to (34)–(36), it is straightforward to express the scattered power as the difference between the extinction power and the absorbed one:

$$P_{\text{sca}} = P_{\text{ext}} - P_{\text{abs}} \tag{37}$$

B. Numerical Simulations

In this subsection, we numerically simulated the NCs optical response by using the Electromagnetic Waves, Frequency Domain module of COMSOL Multiphysics software. The electric field vector was discretized with quadratic Lagrange elements and a frequency domain direct Newton solver ($\tau_d = 1$, $N_{\text{iter}} = 10^3$) was used. Free triangular mesh elements for the NC and the surrounding medium were used, while a swept mesh was used for the perfectly matched layer. We focused on $\omega \in [500, 10000]$ cm^{-1}, with a 100 cm^{-1} step. Numerical simulations are performed on two showcase NCs calling for $t_s = 0$ nm (only core) and $t_s = 4.25$ nm (core-shell structure).

The real and the imaginary part of $\varepsilon(\omega, r)$ obtained from the Drude model by varying ω and the point in the NC are shown in Fig. S2a-d and S2e-h for only core and core-shell NCs, respectively (Supplementary Material). First, we simulated the far-field optical spectra of the NCs from $n_e(r)$ by varying t_s and photodoping conditions, see Figs. 5 a,b and S3 (Supplementary Material). Fig. 5 a shows the corresponding absorption of a single NC calculated using the effective dielectric function of the $t_s = 0$ nm NC, with a peak at 4900 cm^{-1} (2041 nm, in the NIR wavelength region). In the pre-photodoping case (black plot), the spectrum is ruled by strong resonance in the near-infrared region which is likely due to localized surface plasmon resonances resulting from free electrons in the highly doped semiconductor (10^{27} m^{-3}, Fig. 3). After the introduction of charge carriers (post-photodoping, red plot), a stronger localized surface plasmon resonance peak is observed. In the case of the pre-photodoped $t_s = 4.25$ nm NC depicted in Fig. 5 b (black plot) and Fig. S3a (Supplementary Material), we observe a shift of the localized surface plasmon resonance upon shell growth, with a peak at 5300 cm^{-1} (1887 nm – NIR), which is due to the presence of the shell that modifies the dielectric properties of the space surrounding the NC. After photodoping (red plot), two peaks appear in the spectrum (3700 and 5700 cm^{-1} corresponding to 2703 and 1754 nm), indicating a more complex carrier density profile within the core-shell NC which induces an independent resonant mode, generated by a sufficiently high carrier density in the NC shell. These results show that shielding properties can be controlled by changing shell thickness and/or photodoping conditions (Fig. S3, Supplementary Material).

We also simulated the near-field optical properties inside and surrounding the NCs, see Fig. 5 c and d for the core only NC ($t_s = 0$ nm) and Fig. 5 e-j for the core-shell NC ($t_s = 4.25$ nm). We depicted the near-field intensity pattern around the NCs for eight different cases: the electric field evaluated for a NC calling for $t_s = 0$ nm pre- and post-photodoping at the resonance frequency (4900 cm^{-1}) as well as the electric field evaluated for a NC calling for $t_s = 4.25$ nm pre- and post-photodoping at 3700 cm^{-1}, 5300 cm^{-1} and 5700 cm^{-1}, all excited at the maxima localized surface plasmon resonances.

Numerical simulations suggested that the maximum intensity of the electric field is lower for thicker shells and that an increase in the depletion layer leads to a decrease in the maximum near-field intensity when exciting at peak frequencies. It is important to point out that the increased electric field is largely confined within the upper dielectric shell. This loss in near-field enhancement is the result of the stronger contribution of the high refractive index shell. However, near-field excitation at longer wavelengths than the localized surface plasmon resonances peak allows the field confinement to extend to larger sizes and into the surrounding dielectric medium. Although in this case the increase of the maximum field is slightly lower, it provides a solution to overcome the confinement of the field within the NC volume. These effects are further enhanced post-photodoping the NCs, also showing that in the case of a core-shell NC, a splitting of the plasmon resonance occurs due to the presence of two distinct levels of n_e, as shown in Fig. 3, which lead to two distinct frequencies of plasma oscillation.

IV. Conclusion

In this study, we investigated the optical response of ITO-In_2O_3 core-shell nanocrystals in static and dynamic (*i.e.*, photodoping) conditions and for different core-shell architectures, illustrating the evolution of the dielectric function and the absorption peaks in the near-infrared region. Metal oxide nanocrystals are promising candidates to be used for multi-spectral electromagnetic shielding purposes due to their ability to block infrared radiation together with ultraviolet photons, combined with high transparency in the visible range. The experimental results obtained by means of numerical simulations show that the absorption spectrum of doped metal oxide nanoparticles can be engineered both during and after synthesis to better match the targeted electromagnetic interference.

We foresee the development of thin film fabricated by spin-coating ITO-In_2O_3 core-shell nanocrystals with thick shells (*i.e.*, $t_s > 3$ nm) and subsequently photodoped with ultraviolet treatments, as effective shielding coating for transparent screens for vehicles, aircraft and for the next-generation electronic devices. Moreover, similar colloidally-stable doped metal oxide nanocrystals, adapted to be environmentally friendly and skin-compatible, could be employed as photoprotective topical products (*e.g.*, sunscreens) to shield ultraviolet radiation via absorption, preventing sunburns and several kinds of skin cancer.

IV. Supplementary Data

All the data generated in this study has been deposited in the Zenodo database under accession code https://doi.org/10.5281/zenodo.7193366.

References

[1] D. Wanasinghe and F. Aslani, "A review on recent advancement of electromagnetic interference shielding novel metallic materials and processes," *Composites Part B: Eng.*, vol. 176, 2019, Art. no. 107207.

[2] M. Kohani and M. Pecht, "Malfunctions of medical devices due to electrostatic occurrences Big Data analysis of 10 years of the FDA's reports," *IEEE Access*, vol. 6, pp. 5805–5811, 2017.

[3] Y. Chen, H.-B. Zhang, Y. Yang, M. Wang, A. Cao, and Z.-Z. Yu, "High-performance epoxy nanocomposites reinforced with three-dimensional carbon nanotube sponge for electromagnetic interference shielding," *Adv. Funct. Mater.*, vol. 26, no. 3, pp. 447–455, 2016.

[4] D. He et al., "Multispectral electromagnetic shielding using ultra-thin metal-metal oxide decorated hybrid nanofiber membranes," *Commun. Mater.*, vol. 2, no. 1, pp. 1–9, 2021.

[5] F. Shahzad et al., "Electromagnetic interference shielding with 2D transition metal carbides (MXenes)," *Science*, vol. 353, no. 6304, pp. 1137–1140, 2016.

[6] Y.-J. Wan, P.-L. Zhu, S.-H. Yu, R. Sun, C.-P. Wong, and W.-H. Liao, "Anticorrosive, ultralight, and flexible carbon-wrapped metallic nanowire hybrid sponges for highly efficient electromagnetic interference shielding," *Small*, vol. 14, no. 27, 2018, Art. no. 1800534.

[7] L.-Q. Xie et al., "A highly sensitive dopamine sensor based on a polyaniline/reduced graphene oxide/nafion nanocomposite," *Chin. Chem. Lett.*, vol. 28, no. 1, pp. 41–48, 2017.

[8] H.-B. Zhao, Z.-B. Fu, H.-B. Chen, M.-L. Zhong, and C.-Y. Wang, "Excellent electromagnetic absorption capability of Ni/carbon based conductive and magnetic foams synthesized via a green one pot route," *ACS Appl. Mater. Interfaces*, vol. 8, no. 2, pp. 1468–1477, 2016.

[9] R. K. Mishra, M. G. Thomas, J. Abraham, K. Joseph, and S. Thomas, "Electromagnetic interference shielding materials for aerospace application: A state of the art," in *Advanced Materials for Electromagnetic Shielding: Fundamentals, Properties, and Applications*, M. Jaroszewski, S. Thomas, and A. V. Rane, Eds. Hoboken, NJ, USA: Wiley, 2018, pp. 327–365.

[10] Y. Kim, S. Park, and Y. Seo, "Enhanced X-ray shielding ability of polymer–nonleaded metal composites by multilayer structuring," *Ind. Eng. Chem. Res.*, vol. 54, no. 22, pp. 5968–5973, 2015.

[11] S. H. Lee et al., "Density-tunable lightweight polymer composites with dual-functional ability of efficient EMI shielding and heat dissipation," *Nanoscale*, vol. 9, no. 36, pp. 13432–13440, 2017.

[12] M. Li, B. Muneer, Z. Yi, and Q. Zhu, "A broadband compatible multi-spectral metamaterial absorber for visible, near-infrared, and microwave bands," *Adv. Opt. Mater.*, vol. 6, no. 9, 2018, Art. no. 1701238.

[13] X. A. Zhang et al., "Dynamic gating of infrared radiation in a textile," *Science*, vol. 363, no. 6427, pp. 619–623, 2019.

[14] S. Zhong, W. Jiang, P. Xu, T. Liu, J. Huang, and Y. Ma, "A radar-infrared bi-stealth structure based on metasurfaces," *Appl. Phys. Lett.*, vol. 110, no. 6, 2017, Art. no. 0 63502.

[15] C. Cole, T. Shyr, and H. Ou-Yang, "Metal oxide sunscreens protect skin by absorption, not by reflection or scattering," *Photodermatol., photoimmunol. Photomedicine*, vol. 32, no. 1, pp. 5–10, 2016.

[16] M. Ghini, N. Curreli, A. Camellini, M. Wang, A. Asaithambi, and I. Kriegel, "Photodoping of metal oxide nanocrystals for multi-charge accumulation and light-driven energy storage," *Nanoscale*, vol. 13, no. 19, pp. 8773–8783, 2021.

[17] N. Hano, M. Takafuji, H. Noguchi, and H. Ihara, "Monodisperse surface-charge-controlled black nanoparticles for near-infrared shielding," *ACS Appl. Nano Mater.*, vol. 2, no. 6, pp. 3597–3605, 2019.

[18] C. Zhang et al., "An ultralight and thin metasurface for radar-infrared bi-stealth applications," *J. Phys. D: Appl. Phys.*, vol. 50, no. 44, 2017, Art. no. 444002.

[19] B. Fu et al., "Nonlinear optical properties of AG nanoplates plasmon resonance and applications in ultrafast photonics," *J. Lightw. Technol.*, vol. 39, no. 7, pp. 2084–2090, 2021.

[20] M. Alam and Y. Massoud, "A closed-form analytical model for single nanoshells," *IEEE Trans. Nanotechnol.*, vol. 5, no. 3, pp. 265–272, 2006.

[21] P. Ylä-Oijala, D. C. Tzarouchis, E. Raninen, and A. Sihvola, "Characteristic mode analysis of plasmonic nanoantennas," *IEEE Trans. Antennas Propag.*, vol. 65, no. 5, pp. 2165–2172, 2017.

[22] D. C. Tzarouchis and A. Sihvola, "General scattering characteristics of resonant core–shell spheres," *IEEE Trans. Antennas Propag.*, vol. 66, no. 1, pp. 323–330, 2017.

[23] D. Tzarouchis and A. Sihvola, "Light scattering by a dielectric sphere: Perspectives on the Mie resonances," *Appl. Sci.*, vol. 8, no. 2, 2018, Art. no. 184.

[24] A. Mahmood, M. Alam, and Y. Massoud, "A dynamic approach to the lumped impedance representation of a nanoparticle," *IEEE Photon. J.*, vol. 10, no. 4, pp. 1–9, Aug. 2018.

[25] A. Hanif, A. Mahmood, M. Alam, and Y. Massoud, "A compact impedance model of plasmonic nanoshell for metamaterial applications," *IEEE Trans. Nanotechnol.*, vol. 18, pp. 955–962, 2019.

[26] G. Crotti, A. Schirato, R. P. Zaccaria, and G. Della Valle, "On the limits of quasi-static theory in plasmonic nanostructures," *J. Opt.*, vol. 24, no. 1, 2021, Art. no. 015001.

[27] M. Alam and G. V. Eleftheriades, "Multimode impedance representation of scattering, absorption and extinction cross-sectional areas for plasmonic nanoparticles," *J. Lightw. Technol.*, vol. 29, no. 17, pp. 2512–2526, Sep. 2011.

[28] M. U. Khan, A. Kousar, M. Alam, and Y. Massoud, "Closed form resonance solution in metallic nanoparticles with cubic nonlinearity," *IEEE Trans. Nanotechnol.*, vol. 19, pp. 461–468, 2020.

[29] M. Kupresak, X. Zheng, G. A. Vandenbosch, and V. Moshchalkov, "Benchmarking of software tools for the characterization of nanoparticles," *Opt. Exp.*, vol. 25, no. 22, pp. 26760–26780, 2017.

[30] M. Li and Y. Hu, "Simulation of surface enhanced Raman scattering from nanoparticles with wideband nested equivalence source approximation," *IEEE J. Multiscale Multiphys. Comput. Techn.*, vol. 7, pp. 1–8, 2022.

[31] G. P. Szakmany, A. O. Orlov, G. H. Bernstein, M. Lin, and W. Porod, "Multiphysics THz antenna simulations," *IEEE J. Multiscale Multiphys. Comput. Techn.*, vol. 3, pp. 289–294, 2018.

[32] Z. Chen, C.-F. Wang, and W. J. R. Hoefer, "A unified view of computational electromagnetics," *IEEE Trans. Microw. Theory Techn.*, vol. 70, no. 2, pp. 955–969, Feb. 2022.

[33] C. R. Conti III, J. R. McBride, and G. F. Strouse, "Examining the effect of dopant ionic radius on plasmonic m: Zno nanocrystals (m= al3, ga3, in3)," *J. Phys. Chem. C*, vol. 125, no. 14, pp. 7772–7779, 2021.

[34] A. Sheverdin and C. Valagiannopoulos, "Core-shell nanospheres under visible light: Optimal absorption, scattering, and cloaking," *Phys. Rev. B*, vol. 99, no. 7, 2019, Art. no. 075305.

[35] A. Monti, F. Bilotti, and A. Toscano, "Optical cloaking of cylindrical objects by using covers made of core–shell nanoparticles," *Opt. Lett.*, vol. 36, no. 23, pp. 4479–4481, 2011.

[36] M. Ghini et al., "Control of electronic band profiles through depletion layer engineering in core–shell nanocrystals," *Nature Commun.*, vol. 13, no. 1, pp. 1–9, 2022.

[37] R. Seiwatz and M. Green, "Space charge calculations for semiconductors," *J. Appl. Phys.*, vol. 29, no. 7, pp. 1034–1040, 1958.

[38] M. Rudan, *Physics of Semiconductor Devices*. Berlin, Germany: Springer, 2015.

[39] P. Rhodes, "Fermi-dirac functions of integral order," *Proc. Roy. Soc. London. Ser. A. Math. Phys. Sci.*, vol. 204, no. 1078, pp. 396–405, 1950.

[40] S. M. Sze, Y. Li, and K. K. Ng, *Physics of Semiconductor Devices*. Hoboken, NJ, USA: Wiley, 2021.

[41] F. Garcia-Moliner, "The band picture in the electronic theories of chemisorption on semiconductors," *Catalysis Rev.*, vol. 2, no. 1, pp. 1–66, 1969.

[42] A. Agrawal, I. Kriegel, E. L. Runnerstrom, F. Scotognella, A. Llordes, and D. J. Milliron, "Rationalizing the impact of surface depletion on electrochemical modulation of plasmon resonance absorption in metal oxide nanocrystals," *ACS Photon.*, vol. 5, no. 5, pp. 2044–2050, 2018.

[43] C. K. Brozek, D. Zhou, H. Liu, X. Li, K. R. Kittilstved, and D. R. Gamelin, "Soluble supercapacitors: Large and reversible charge storage in colloidal iron-doped ZnO nanocrystals," *Nano Lett.*, vol. 18, no. 5, pp. 3297–3302, 2018.

[44] A. M. Schimpf, S. D. Lounis, E. L. Runnerstrom, D. J. Milliron, and D. R. Gamelin, "Redox chemistries and plasmon energies of photodoped In2O3 and Sn-doped In2O3 (ITO) nanocrystals," *J. Amer. Chem. Soc.*, vol. 137, no. 1, pp. 518–524, 2015.

[45] I. Kriegel et al., "Ultrafast photodoping and plasmon dynamics in fluorine–indium codoped cadmium oxide nanocrystals for all-optical signal manipulation at optical communication wavelengths," *J. Phys. Chem. Lett.*, vol. 7, no. 19, pp. 3873–3881, 2016.

[46] L. Liao, K.-J. Jin, H.-b. Lu, J. Qiu, P. Han, and L.-l. Zhang, "Theoretical study on the photodoping effects in La1–x Srx MnO3/SrNby Ti1–y O3 p–n heterojunction," *Physica Status Solidi(a)*, vol. 206, no. 7, pp. 1655–1659, 2009.

[47] G. V. Hartland, "Optical studies of dynamics in noble metal nanostructures," *Chem. Rev.*, vol. 111, no. 6, pp. 3858–3887, 2011.

[48] A. Agrawal, R. W. Johns, and D. J. Milliron, "Control of localized surface plasmon resonances in metal oxide nanocrystals," *Annu. Rev. Mater. Res.*, vol. 47, pp. 1–31, 2017.

[49] I. Kriegel, F. Scotognella, and L. Manna, "Plasmonic doped semiconductor nanocrystals: Properties, fabrication, applications and perspectives," *Phys. Rep.*, vol. 674, pp. 1–52, 2017.

[50] A. M. Schimpf, N. Thakkar, C. E. Gunthardt, D. J. Masiello, and D. R. Gamelin, "Charge-tunable quantum plasmons in colloidal semiconductor nanocrystals," *ACS Nano*, vol. 8, no. 1, pp. 1065–1072, 2014.

[51] J. D. Jackson, *Classical Electrodynamics*. College Park, MD, USA: Amer. Assoc. Phys. Teachers, 1999.
[52] A. G. Polimeridis, M. H. Reid, S. G. Johnson, J. K. White, and A. W. Rodriguez, "On the computation of power in volume integral equation formulations," *IEEE Trans. Antennas Propag.*, vol. 63, no. 2, pp. 611–620, Feb. 2015.

Nicola Curreli (Member, IEEE) received the M.Sc. degree from the University of Genoa, Genoa, Italy, in 2016, and the Ph.D. degree in electronic engineering from the University of Cagliari, Cagliari, Italy, and the Italian Institute of Technology – IIT, Genoa, in 2020. After completing the Ph.D. degree, he held a Fellow Position with Graphene Labs – IIT within the Graphene Core 2 Project (Graphene Flagship). In 2019, he was a visiting Researcher with the Physics and Mechanical Engineering Departments, Columbia University, New York City, NY, USA, as part of the Marie Sklodowska-Curie SONAR H2020 Action. Between 2022 and 2023, he has been a Visiting Researcher with the Molecular Foundry at Lawrence Berkeley National Laboratory, Berkeley, CA, USA. He is currently a Postdoctoral Researcher with the Functional Nanosystems Group – IIT. His research interests include the study of low-dimensional materials, their characterization, and their application in the field of photonics, and the design, implementation, and analysis of linear and nonlinear integrated optical, microwave devices, and antennas. He was the recipient of the Young Scientists at the General Assembly and Scientific Symposium of URSI in 2022. He is a Member of the Topical Advisory Panel of Photonics.

Matteo Bruno Lodi (Member, IEEE) received the bachelor's degree in biomedical engineering from the University of Cagliari, Cagliari, Italy, in 2016, and the master's degree in biomedical engineering from Politecnico di Torino, Turin, Italy, in 2018, the Ph.D. degree (Hons.) in electronic engineering and computer science from the University of Cagliari in 2022. He is a Technologist with the Applied Electromagnetics Group. His research interests include the modelling of bioelectromagnetic phenomena, especially hyperthermia treatment, the study, manufacturing, and synthesis of magnetic biomaterials for tissue engineering applications, and the use of microwaves for biotechnology and environmental applications, while working with the design and characterization of antennas for space and wearable applications. He was the recipient of the Roberto Sorrentino Young Scientist award at the 2022 Italian URSI Assemblyand Young Scientists at the General Assembly and Scientific Symposium of URSI in 2020 and 2021. He is a Member of the WG2: Better thermal-based EM therapeutics of the COST Action 17115 MyWave. He has been appointed as Representative for the Young Professionals of IEEE Region 8 Nanotechnology Council. He is a Member of the Editorial Board of the IEEE Future Directions Technology Policy and Ethics newsletter, of the *Journal of Food Processing and Preservation* and of the *International Journal of RF and Microwave Computer-Aided Engineering.*

Michele Ghini received the B.Sc. and M.Sc. degress in physics (with Hons.) from the University of Bologna, Bologna,Italy, in 2013 and 2016, respectively, the Ph.D. degree in nanochemistry (with Hons.) from the University of Genova, Genoa, Italy, and the Italian Institute of Technology - IIT, in 2022. After the Ph.D. degree, he held a Fellow Position with the Functional Nanosystems Group (IIT), as part of the ERC project Light-DYNAMO. He was a Visiting Student with the University of Oxford, Oxford,U.K., in 2018 and a Visiting Researcher with Columbia University, New York NY, USA,in 2019. He is currently a Postdoctoral Researcher with the NANOLAB group, École Polytechnique Fédérale de Lausanne, Lausanne, Switzerland His research interests include the study of the unique properties of nanomaterials, their interaction with light, and their application for innovative energy storage solutions, and the fabrication of silicon spin qubits for quantum computing.

Nicolò Petrini received the B.Sc degree in physics engineering (with Hons.) from Politecnico of Torino, Turin, Italy, in 2017, and the M.Sc. joint degree (with Hons.) in nanotechnology for the ICTs from Politecnico di Torino, Grenoble INP (France) and École Polytechnique Fédérale de Lausanne, Lausanne Switzerland, in 2019. In 2019, he was a Visiting Student with the Quantum Nanostructures and Nanofabrication Group, Department of Electrical Engineering and Computer Science, Massachusetts Institute of Technology, Cambridge, MA, USA. He is currently working toward the Ph.D. degree with the University of Genova, Genoa, Italy and Functional Nanosystems Group, Italian Institute of Technology, Genoa, Italy. His research interests include the study of nanostructures composed by low-dimensional materials, their characterization, and their application in the field of nanoelectronics and energy harvesting.

Andrea Buono (Senior Member, IEEE) was born in Naples, Italy, in 1984. He received the B.Sc. and M.Sc. degrees in telecommunication engineering and the Ph.D. degree in information engineering from the Università di Napoli "Parthenope," Naples, Italy, in 2010, 2013 and 2017, respectively. Since 2018, he has been Assistant Professor with the Università di Napoli "Parthenope." His main research include applied electromagnetics, including electromagnetic modeling, bbreak polarimetry, ocean and coastal area applications.

Maurizio Migliaccio (Fellow, IEEE) was born in Naples, Italy, in 1962. He received the Laurea degree (Hons.) in electronic engineering from the Università degli Studi di Naples Federico II, Naples, Italy, in 1987. Since 1994, he has been teaching microwave remote sensing. Since 2005, he has been a Full Professor of electromagnetics with the Università degli Studi di Naples Parthenope, Naples. Since 2013, he has been an Affiliated Full Professor with NOVA Southeastern University, Fort Lauderdale, FL, USA. He has authored or coauthored more than 200 peer-reviewed journal articles on remote sensing and applied electromagnetics. His research interest include applied electromagnetics. Prof. Migliaccio was a Member of the Italian Space Agency Scientific Committee. He is an Associate Editor for the *International Journal of Remote Sensing* and IEEE TRANSACTIONS ON GEOSCIENCE AND REMOTE SENSING.

Alessandro Fanti (Senior Member, IEEE) received the Laurea degree in electronic engineering and the Ph.D. degree in electronic engineering and computer science from the University of Cagliari, Cagliari, Italy, in 2006 and 2012, respectively. From 2013 to 2016, he was a Postdoctoral Fellow of the Electromagnetic Group, University of Cagliari, where he is currently an Assistant Professor. He has authored or coauthored 57 papers in international journals. His research interests include the use of numerical techniques for modes computation of guiding structures, optimization techniques, analysis and design of waveguide slot arrays, analysis and design of patch antennas, radio propagation in urban environment, modeling of bioelectromagnetic phenomena, and microwave exposure systems for biotechnology and bioagriculture. He is a Member of the IEEE Antennas and Propagation Society, Italian Society of Electromagnetism, National Inter-University Consortium for Telecommunications, and Interuniversity Center for the Interaction Between Electromagnetic Fields and Biosystems. He is an Associate Editor for the IEEE JOURNAL OF ELECTROMAGNETICS, RF AND MICROWAVES IN MEDICINE AND BIOLOGY. Since 2020, he has been a Principal Investigator of the IAPC Project, funded with e5 million by the Italian Ministry of Economic Development (MISE), within the AGRIFOOD PON I&C 2014-2020 (CUP: B21B1900064008 COR: 1406652).

Ilka Kriegel received the M.Sc. degree in advanced materials science from Technical University Munich, Munich, Germany, in 2009, accompanied by a research stay with the University of Chicago, Chicago, IL, USA, in 2010, and the Ph.D. degree in physics from Technical University Munich, in 2013. During her first Postdoc with Politecnico di Milano, Milan, Italy, she delved into the ultrafast spectral response of hybrid nanomaterials. She is currently the Head of the Functional Nanosystems Group, IIT and holds an ERC Starting Grant (Light-DYNAMO). She is also coordinator of a proactive FET collaborative grant (LIGHT-CAP). Her main research interests include the exploitation of functional nanosystems for energy and the environment. A Marie-Curie fellowship (global) brought her to the Molecular Foundry, Lawrence Berkeley National Laboratory, Berkeley, CA, USA, and the Italian Institute of Technology (IIT), Genoa, Italy, extending her knowledge to two-dimensional materials.

Giuseppe Mazzarella (Senior Member, IEEE) received the Graduation degree (*Summa with Laude)* in electronic engineering and the Ph.D. degree in electronic engineering and computer science from the Università Federico II of Naples, Naples, Italy, in 1984 and 1989, respectively. In 1990, he became an Assistant Professor with the Dipartimento di Ingegneria Elettronica, Università Federico II of Naples. He has been with the Dipartimento di Ingegneria Elettrica ed Elettronica, Università di Cagliari, first as an Associate Professor since 1990, and then a Full Professor, teaching courses in electromagnetics, microwave, antennas and remote sensing since 2000. His research interests include efficient design of large arrays of slots, power synthesis of array factor, with emphasis on inclusion of constraints, microwave holography techniques for the diagnosis of large reflector antennas, use of evolutionary programming for the solution of inverse problems, and in particular problems of synthesis of antennas and periodic structures. He is the author or coauthor of more than 100 papers in international journals. He is a Reviewer of many EM journals.

Open Access provided by 'Università degli Studi di Cagliari' within the CRUI CARE Agreement